Field application of close-range digital photogrammetry (CRDP) for grain-scale fluvial morphology studies

Stéphane Bertin, Heide Friedrich

Field application of close-range digital photogrammetry (CRDP) for grain-scale fluvial morphology studies

Stephane Bertin and Heide Friedrich, Department of Civil and Environmental Engineering, The University of Auckland, Auckland, New Zealand.

Corresponding author: S. Bertin, Department of Civil and Environmental Engineering, The University of Auckland, Auckland, New Zealand (s.bertin@ymail.com).

Abstract (up to 300 words)

In situ measurement of grain-scale fluvial morphology is important for studies on grain roughness, sediment transport and the interactions between animals and the geomorphology, topics relevant to many river practitioners. Close-range digital photogrammetry (CRDP) and terrestrial laser scanning (TLS) are the two most common techniques to obtain high-resolution digital elevation models (DEMs) from fluvial surfaces. However, field application of topography remote sensing at the grain scale is presently hindered mainly by the tedious workflow challenges that one needs to overcome to obtain high-accuracy elevation data. A recommended approach for CRDP to collect high-resolution and high-accuracy DEMs has been developed for gravel-bed flume studies. The present paper investigates the deployment of the laboratory technique on three exposed gravel bars in a natural river environment. In contrast to other approaches, having the calibration carried out in the laboratory removes the need for independently surveyed ground-control

targets, and makes for an efficient and effective data collection in the field. Optimisation of the gravel-bed imagery helps DEM collection, without being impacted by variable lighting conditions. The benefit of a light-weight 3D-printed gravel-bed model for DEM quality assessment is shown, and confirms the reliability of grain roughness data measured with CRDP. Imagery and DEM analysis evidences sedimentological contrasts between gravel bars within the reach. The analysis of the surface elevations shows the effect variable grain-size and sediment sorting have on the surface roughness. By plotting the 2D structure functions and surface slopes and aspects we identify different grain arrangements and surface structures. The calculation of the inclination index allows determining the surface-forming flow direction(s). We show that progress in topography remote sensing is important to extend our knowledge on fluvial morphology processes at the grain scale, and how a technique customised for use by fluvial geomorphologists in the field benefits this progress.

Keywords (5)

Field work; Gravel-bed river; Photogrammetry; DEM; Grain roughness

1. Introduction

Studies on the geomorphology of gravel-bed rivers at the grain scale and the measurement of gravel patches have seen a growing interest over the last decades, due to progress in high-resolution remote sensing. Digital elevation models (DEMs), analysed using the standard deviation of bed elevations, can potentially replace tedious sediment sampling in the field and improve grain-roughness parameterisation needed for hydraulic and sediment transport calculations (Aberle

48 and Smart, 2003; Entwistle and Fuller, 2009; Heritage and Milan, 2009; Nikora et al.,
49 1998). Likewise, collection of high-resolution DEMs from distinct hydraulic biotopes
50 (e.g. riffles and pools, or bars and pools, exposed at the time of measurement) was
51 critical in characterising the links between morphological units, sediment transport
52 and surface structure (Hodge et al., 2009a; Hodge et al., 2013) and to quantify the
53 “patchy” nature of gravel surfaces (Nelson et al., 2010). With only traditional field
54 sampling of surface composition, crucial information on particle exposure,
55 imbrication and surface roughness cannot be derived. Measuring microtopographic
56 relief is also important as it provides means to assess aquatic habitats and the
57 relation between species and the geomorphology (Du Preez and Tunnicliffe, 2012;
58 Hannam and Moskal, 2015; Rice et al., 2012).

59 Close-range digital photogrammetry (CRDP), i.e. the combination of using one or
60 more digital cameras and subsequent image matching to obtain surface elevations at
61 the image overlap, and “time-of-flight” terrestrial laser-scanning (TLS), are presently
62 the most commonly used remote-sensing techniques, able to measure gravel-bed
63 topography with a sufficient amount of detail at the grain scale (spatial resolution
64 ~mm). Both techniques have been used in both laboratory and field settings, and
65 have been shown capable of measuring shallow riverbed microtopography (Bertin et
66 al., 2013; Butler et al., 2002; Smith et al., 2012; Smith and Vericat, 2013). However,
67 the latter is seldom used, mainly due to degraded DEM quality compared to
68 conventional in-air measurement. In addition, this application comes with substantial
69 experimental difficulties. Generally, studied surfaces are exposed gravel bars at low
70 flow or in drained laboratory flumes. When it comes to field applications, various
71 methodological attributes may be considered to decide which technique to adopt.
72 The most important aspect is the need to obtain fit-for-purpose topography data,

which are suitable for the intended analysis. In other words, what is a sufficient measurement accuracy and precision to improve our knowledge of fluvial microtopography? For measuring fluvial surfaces at the grain scale, both CRDP and TLS methodologies require the greatest care to mitigate errors in elevation data (Bertin et al., 2015; Hodge et al., 2009b), errors which otherwise may affect findings (James et al., 2007; Lane et al., 2005). Repeating scans, in addition to applying erroneous points filtering techniques (Hodge et al., 2009b), is currently the best option to reduce errors and improve accuracy for TLS applications, with the measuring precision otherwise being dependent on the used instrument and software. The challenge with CRDP is the development of a stable workflow from image acquisition to surface structure data (Chandler et al., 2005; Lane, 2000; Lane et al., 2000; Wackrow et al., 2007). Presently, a variety of DEM reconstruction techniques are available, from the now conventional digital stereo (i.e. two-camera) photogrammetry, using either commercial (Bird et al., 2010; Butler et al., 2002; Chandler et al., 2005; Lane, 2000; Lane et al., 2000) or non-proprietary (Bertin et al., 2013; Bertin et al., 2014; Bertin et al., 2015; Bouratsis et al., 2013) calibration and stereo-matching engines, to novel structure-from-motion (SfM) or multi-view stereo (MVS) photogrammetry (Fonstad et al., 2013; James and Robson, 2012; Javernick et al., 2014), which does not need calibration but has not been tested on a gravel patch yet. Recent progress was made in the laboratory, showing that the use of non-proprietary digital stereo photogrammetry optimises the workflow, which when done appropriately, can result in sub-millimetre accurate gravel-bed DEMs (Bertin et al., 2015) - a development that is yet to be tested in a natural river environment. Compared to applying CRDP in the laboratory, the ease with which data are collected in the field is also becoming more important, in addition to the quality of

98 obtained data. A well-developed CRDP system has the advantage of being easily
99 deployed in the field due to its reduced cost, its small size and weight, its optional
100 power supply and the possibility of very quick data collection (Bird et al., 2010;
101 Javernick et al., 2014; Lane, 2000; Rieke-Zapp et al., 2009).

102 Despite the wealth of available photogrammetric solutions, and the possibility to
103 provide a lightweight and very accurate surveying equipment customised for use by
104 earth scientists, “potential photogrammetric users continue to have reservations
105 about its potential and often consider its field use to be too complicated” (Rieke-Zapp
106 et al., 2009). In response, this paper presents an example of how CRDP can be
107 used in the field to collect information on fluvial microtopography efficiently and
108 effectively. We tested a recently developed non-proprietary CRDP technique (Bertin
109 et al., 2015), for which the imaging system relies on two consumer-grade digital
110 cameras, in a field environment, measuring exposed gravel bars at the grain scale. A
111 small meandering gravel-bed river in New Zealand was the location for the tests.
112 Imagery data were collected at three distinct gravel bars, allowing testing in a variety
113 of sediment size and surface structure settings. A ground-truth object was used on
114 site to assess the accuracy of obtained elevation data, generally performed in other
115 studies using an independent measuring device. CRDP readily produced sub-
116 millimetre resolution and accuracy DEMs, without the need to deploy control targets
117 on the riverbed for calibration. Using CRDP has the advantage that calibration of the
118 cameras can be carried out in the laboratory before going to the field. We show that
119 by doing so, DEM collection is not affected negatively with test undertaken on the
120 field site. Information derived from the CRDP data was adequate to monitor surface
121 roughness, grain size and 3D arrangement. Ultimately, this allowed examination of
122 the sedimentological contrasts between bars within the reach.

2. Methodology

2.1. Study site: the Whakatiwai river

Field data were collected from the Whakatiwai river (**Figure 1A**), located in the North Island of New Zealand (37° 05' S, 175° 18' E), a small gravel-bed river flowing over greywacke material and draining a watershed of ~12 km^2 (maximum elevation c. 490 m amsl). The Whakatiwai is fed by numerous small streams originating from the steep East-facing slopes of the Hunua Ranges, and flows to sea in a very short distance, roughly ten kilometres from its source to the river mouth in the Firth of Thames. On the valley floor, the Whakatiwai is a meandering river, with rapid alluvium bank erosion during flood flows, which essentially transports cobbles (5-25 cm) and pebbles (1-5 cm), with occasional patches of sand/silt and small boulders found along its bed. Because of its short span, there is no gravel-sand transition; the riverbed remains gravelly all the way through to the river mouth. In terms of hydrologic regime, the Whakatiwai is governed by flashy hydrographs and competent flows during the autumn-spring season, with mostly low flows over the summer months, during which gravel bars become vegetated. No flow gauging exists for the river; hence flow data are unavailable for the site.

For the tests a ~200 m long study reach was chosen, situated only hundred meters upstream of the river mouth and comprising numerous well-defined gravel bars adjacent to the eroding banks. Three exposed and vegetation-free gravel bars were selected, covering a range of sediment size and surface structures. They were labelled bar #1 to #3, with numbers increasing upstream. Within each bar, a small area of exposed gravel (~ 0.5 m^2), termed "patch", was chosen at the bar head close to the water edge, for consistency in the measurements, also ensuring the surfaces studied are regularly water-worked.

A

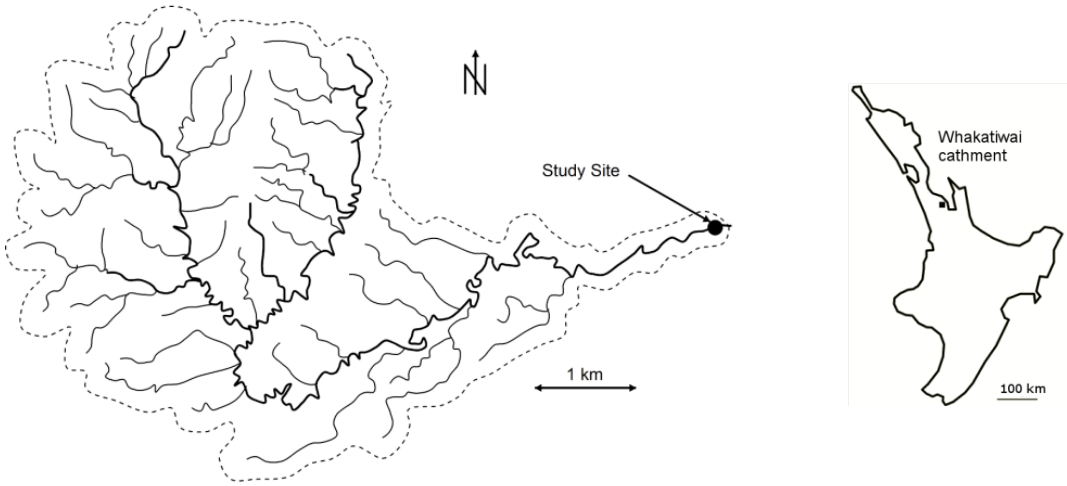

B

148 ***Figure 1.*** *Whakatiwai catchment in the North Island of New Zealand, A) site location;*
149 *and B) image of CRDP deployment on Bar #2, looking upstream. Note the alignment*
150 *of the setup with the apparent flow direction.*

151 ## 2.2. CRDP deployment and field DEM collection

152 Imagery data were collected from the three patches in August 2014, after an
153 extended period of dry weather, following a methodology developed in the laboratory
154 and presented in Bertin et al. (2015). The two cameras used in stereo (side-by-side,
155 separated by a 250 mm baseline distance between the two optical centres) were
156 Nikon D5100s (16.2 Mpixel complementary metal oxide semiconductor (CMOS)
157 sensors) with Nikkor 20 mm lenses. The cameras, fully charged, were rigidly
158 attached on a 1.2 m long mounting bar that could be hanged horizontally (using a

159 bubble level) above the riverbed using two tripods (**Figure 1B**). The setup (cameras,
160 tripods and mounting bar) weighed approximately 8 Kg.

161 Prior to transport to the field, the cameras' arrangement on the mounting bar was
162 carefully calibrated in the laboratory by recording stereo photographs (also called
163 stereoscopic images) of a flat chequerboard, and using Bouguet (2010)'s Matlab®
164 toolbox to determine the calibration parameters (readers should refer to Bertin et al.
165 (2015) for a complete description of the calibration process). The aperture was set to
166 f/20, ensuring a large depth of field, and focus was set at a distance of 0.8 m, based
167 on the expected field requirements. After calibration, care was taken to ensure that
168 the cameras' arrangement (i.e. relative rotation and translation) was not disturbed.
169 Subsequent testing in the field, after transport, confirmed that minimal disturbance
170 occured.

171 Whilst in the field, we attempted to orientate the mounting bar parallel to the
172 antecedent flow direction (**Figure 1B**), determined by eye from channel shape,
173 producing photographs and DEMs with *x*-axis values increasing downstream (e.g.
174 **Figure 3**). This later allowed to relate the measured bed properties to the local flow
175 direction. Stereo photographs of the exposed patches were recorded vertically,
176 reducing occlusions (i.e. shadowed areas that cannot be seen in one or the two
177 images) on the surface compared with oblique measurements, from a height of
178 approximately 0.8 m, resulting in point data spacing (i.e. pixel size) ~0.2 mm and a
179 theoretical depth resolution ~0.6 mm. Cameras were operated in manual mode, with
180 the possibility to vary the shutter speed to have well-illuminated and contrasted
181 photographs necessary for successful stereo matching (Bertin et al., 2015). Remote
182 control was possible by connecting the cameras to a laptop.

Data processing consisted in rectifying the stereo photographs to epipolar geometry using the calibration parameters, and transforming the images with the multi-scale Retinex algorithm in GIMP®, before pixel-to-pixel stereo matching using Gimel'farb (2002)'s SDPS, providing point cloud data and ortho-images. Because the SDPS algorithm matches corresponding points along lines of 1 pixel width, accurate image rectification (hence accurate calibration) is essential to produce stereo photographs whose corresponding pixels are ideally on the same scanline (also called epipolar lines, i.e. same vertical position in a photograph). Doing so minimises the systematic matching errors due to calibration. Image transformation with Retinex heightens the similarity between the two images forming a stereo photograph and improves stereo-matching performance (Bertin et al., 2015), which is specifically important in the field application lacking direct control over the illumination. From the point cloud data, DEMs were interpolated onto regular grids with 1 mm spacing, first by interpolating onto 0.25 mm grids, consistent with the best resolution achievable, to minimise the loss of topographic information (Bertin et al., 2014; Hodge et al., 2009b), then resampling onto the final grids to expedite calculations with minimal surface smoothing (mean unsigned (absolute) error, MUE ~0.025 mm and standard deviation of error, SDE ~0.035 mm between initial and resampled surfaces). Before resampling onto a 1 mm grid, outliers were identified using the mean elevation difference parameter (Hodge et al., 2009b), and replaced in the DEMs using bi-cubic spline interpolation. Because the MUE between original and filtered DEMs accounted for less than 0.01 mm, filtering was considered optional and its application was not stringent.

2.3. CRDP validation and field DEM accuracy

CRDP data quality assessment was done in two ways, by (i) checking on site the validity of the calibration performed in the laboratory prior to moving to the field; and (ii) measuring a ground-truth object, to realistically determine the accuracy of the field DEMs.

To ascertain the validity of the calibration performed in the laboratory, after having transported the CRDP setup to the field, a small chequerboard (0.3 x 0.2 m, ~0.2 Kg, made of alternating black and white squares) was placed on the riverbed and photographed in different positions, altogether covering the common field of view (CFoV) between both cameras. The stereo photographs were rectified using the calibration data obtained in the laboratory, and the rectification error, which is the absolute scanline difference between corresponding pixels (Bertin et al., 2015; Bradley and Heidrich, 2010), was measured for every square's corners in all rectified stereo photographs of the chequerboard (i.e. at about 200 locations throughout the measurement area). The mean, standard deviation, and maximum rectification error were computed, and compared with values obtained before moving to the field.

Final DEM quality was assessed by measuring a 3D-printed gravel bed, specifically transported to the field, following the method of Bertin et al. (2014). The use of this realistic ground-truth object of a water-worked gravel bed improves on previous DEM assessment methods, traditionally requiring check points to be deployed on the riverbed and surveyed with a total station, to be able to compare with the measurements after co-registration of the two (Bouratsis et al., 2013; Butler et al., 1998; Lane, 2000; Lane et al., 2000), in terms of density/repartition of the check points and registration errors, hence reliability of the assessment. We show herewith that the field use of the 3D-printed gravel bed ground truth sped up and

made DEM quality assessment easier. For the assessment, the 3D-printed gravel bed model (296 x 184 mm, ~1.5 Kg, shown in **Figure 4**) was imaged with CRDP besides gravel-bar microtopography (same camera distance of 0.8 m). After DEM reconstruction, measured elevations were aligned with the 'truth' elevations and compared at more than 800,000 points, located every 0.25 mm on an orthogonal grid, to realistically determine the field performance of CRDP in this work.

2.4. DEM analysis and information on gravel-bar surface structure

Before the DEMs were analysed, it was necessary to remove the combined effect of the local bed slope and setup misalignment from the riverbed (i.e. non-parallelism), which could obscure smaller grain-scale properties. In the absence of bedforms, linear trend surfaces were removed from the DEMs using a least-squares fit procedure (Aberle and Nikora, 2006; Cooper and Tait, 2009; Hodge et al., 2009a), and DEMs were normalised to have a mean elevation equal to zero.

Analysis of gravel-bar topography and surface structure started with the calculation of first-order moments of detrended bed elevations: the range (Δ_Z), standard deviation (σ_Z) and skewness (S_k) were evaluated. The first two parameters are surrogates of grain roughness parameters based on sediment size (Aberle and Smart, 2003; Entwistle and Fuller, 2009; Heritage and Milan, 2009; Nikora et al., 1998). The bed elevation skewness is useful to determine if a gravel bed is water-worked, in this case displaying positive values, contrasting with the negatively skewed man-made screeded gravel beds (Aberle and Nikora, 2006). Generalised 2D second-order structure functions (Nikora et al., 1998), similar to using semivariograms, were used to estimate the correlations between detrended elevations at different lags and in different directions. DEM analysis continued with the evaluation of the slope and aspect angles of each of the 1 mm^2 DEM grid cells

256 (Hodge et al., 2009a), providing information on grain arrangement at the bar surface.
257 The last step in our investigation of DEM properties was the evaluation of the
258 inclination index, representing particle imbrication, which should be maximal in the
259 direction of the flow (Laronne and Carson, 1976), by analysing the signs of elevation
260 changes between successive pairs of DEM points at different lags and in different
261 directions, following the method presented in Millane et al. (2006). Information on
262 how to use these different statistical analysis methods applied to the DEMs is
263 introduced in detail in the references provided, and thus is not repeated herewith.

264 ## 2.5. Image analysis and information on bed-surface grain size and
265 orientation

266 To complement information derived from the DEMs, grain-size distributions (GSDs)
267 based on the sediment grains' intermediate (*b*-) axis, and the grains' long (*a*-) axis
268 orientation, were determined using the image-analysis tool Basegrain®, which allows
269 for automatic grain separation in digital pictures of gravel beds and applies Fehr's
270 (1987) line-sampling method for the results' analysis (Detert and Weitbrecht, 2012).
271 For each patch, a single photograph collected with CRDP was necessary.

272 In order to determine the bed-surface composition (and not the subsurface
273 composition, as per default), the percentage of non-detected fines at 10 mm was
274 changed from 25% to 10% during the results' analysis, as in Rüther et al. (2013).
275 Moreover, the ratio of image-detected *b*-axis (written *b'*) and true *b*-axis, which
276 generally differs from unity due to particle burial, foreshortening and overlapping
277 (Graham et al., 2010), was adjusted to obtain GSDs comparable with GSDs obtained
278 by manual size-sieving. *b/b'* was calibrated by measuring gravels picked up along a
279 line on the riverbed with a digital calliper, and comparing the results with those
280 obtained by Basegrain®. The best match was obtained using *b/b'* = 1.19, a value

281 also reported from armour layers formed in a laboratory flume (Bertin and Friedrich,
282 Submitted). Grain orientation was automatically determined by fitting an ellipse,
283 whose areal normalised second-central moment equals that of the grain, and by
284 computing the angle formed between the ellipse long axis and the flow-orientated
285 image long axis.

286 ## 3. Field observations and analysis

287 ### 3.1. Bed-surface grain size and orientation

288 The three patches examined present large differences in sediment size at the bar
289 surface (**Figures 2A and 3**). The median sediment size (D_{50}) varied between 18 and
290 47 mm; D_{16} between 7 and 18 mm; and D_{90} between 27 and 104 mm. The patch in
291 bar #1 was the better sorted of the three patches, with a geometric standard
292 deviation $\sigma = \sqrt{D_{84}/D_{16}} = 1.4$, compared with 2.2 and 2.4 for bar #2 and bar #3,
293 respectively. Grain-size variability between gravel bars in the same river reach is not
294 surprising (e.g. Hauer et al. (2014) and Verdú et al. (2005)). Grain-size variability
295 within bars was also recognised, with coarser material found at the bar head
296 compared to the bar tail (D_{50} increased by 30% in average, Rice and Church (2010)).
297 Despite that consistent patch selection at the bar head was not easily achieved in
298 practice, the between-bar grain-size differences observed in **Figure 2A** largely
299 exceed the in-bar variability observed by Rice and Church (2010), indicating a neat
300 grain-size difference between bars in the Whakatiwai that is not the result of
301 downstream fining only. It is assumed that this difference arises from a combination
302 of factors, such as the elevation of the patch with respect to the mean water-surface
303 level, the planform position of the gravel bar, consistent with competence

304 considerations (Rice and Church, 2010), and the chute of sediment from the eroding
305 banks.

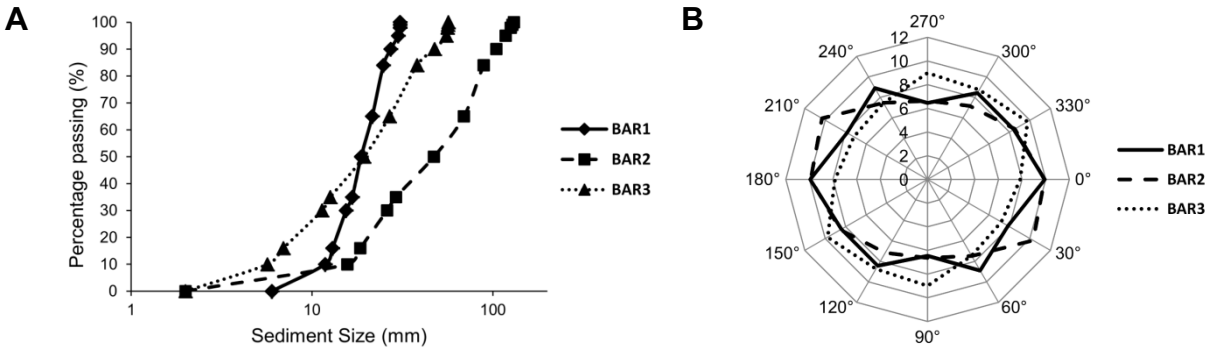

306 ***Figure 2.*** *(A) Bed-surface grain-size distributions for the three Whakatiwai patches;*
307 *and (B) frequency-distribution of grains' a-axis (i.e. long axis) orientation with respect*
308 *to the flow direction determined by eye in the field (from 0° to 180°).*

309 Grain orientation at the bed surface also differed between patches (**Figure 2B**).
310 For bar #1, the bed material preferentially aligned its long axis parallel to the flow
311 direction. This preferential alignment of the grains with water-working, linked to an in-
312 situ reworking of grains in below entrainment threshold conditions, was observed
313 previously (Aberle and Nikora, 2006; Butler et al., 2001). For bar #2, the same
314 preferential alignment of the grains was observed, but this time, the proportion of
315 grains forming a 30° angle to the flow with their *a*-axis was as large as the proportion
316 of grains aligned parallel to the flow. This may suggest that the actual surface-
317 forming flow direction was somewhere between 0° and 30° with respect to the image
318 orientation. The latter analysis should be taken with caution however, as previous
319 research showed that prevailing grain orientation is also influenced by the sediment
320 transport mode, hence is an ambiguous descriptor of flow direction (Hodge et al.,
321 2009a). For instance, coarse grains transported by rolling or sliding often come to
322 rest with their a-axis perpendicular to the flow direction (Laronne and Carson, 1976).

Bar #3 presents the largest proportion of grains aligned perpendicular to the (assumed) flow direction. There are two possibilities to explain this tendency: the flow direction was not correctly determined; or, more coarse grains were transported by rolling or sliding during the last competent event(s) compared to the other patches.

3.2. Grain-scale DEMs and ortho-images

CRDP naturally produces 2D (i.e. ortho-images) and 2.5D (i.e. DEMs) maps of the surfaces studied (**Figure 3**). In previous studies, visualisation of the ortho-images, and comparison with the DEMs, was considered an effective way of controlling photogrammetric performance qualitatively (Butler et al., 1998; Lane, 2000). Since visual inspection of the ortho-images obtained during this work show high quality (**Figure 3**), without apparent mixed pixels and/or distortions, we can assume that stereo matching performed well for the entire measurement area.

Field studies using TLS also require imagery data to be collected, whether it is for documenting (Heritage and Milan, 2009) and/or for grain-size analysis (Hodge et al., 2009a). As CRDP data are obtained from imagery, both the DEMs and the ortho-images are automatically referenced within the same coordinate system (**Figure 3**), which saves the need to align the two.

3.3. CRDP validation and DEM accuracy

The rectification error just after calibration (i.e. in the laboratory) was represented by a mean of 0.09 pixel, a standard deviation of 0.08 pixel and a maximum of 0.37 pixel, ensuring minimal systematic error during stereo matching. After moving the CRDP setup to the field, the rectification error increased (mean = 0.29 pixel, standard deviation = 0.23 pixel and maximum = 0.91 pixel), certainly caused by the transport

(and shaking that occurred) in the car. It is noted that no particular measure was taken to transport the setup; other than it being placed flat in the boot of the car, surrounded by

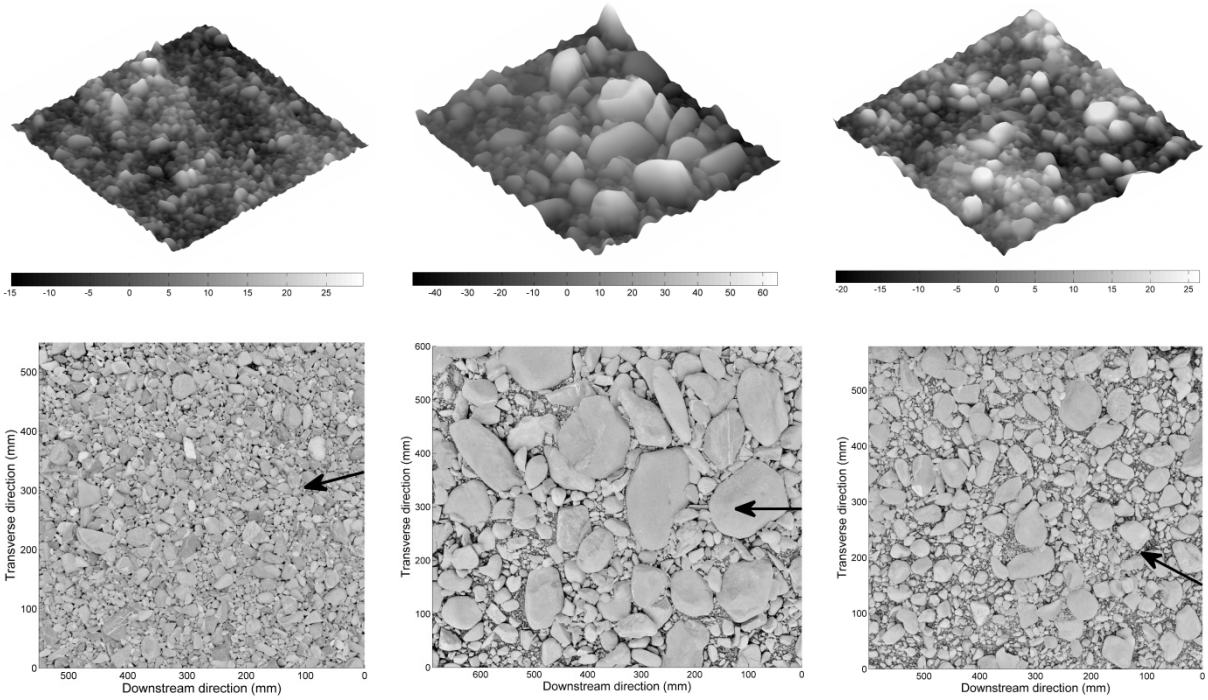

Figure 3. *Final DEMs and ortho-images from the Whakatiwai patches (bar #1 to #3 from left to right). Elevation is represented as gradient of greys, and is in millimetres. Flow direction, determined visually in the field, is from right to left. Arrows show the most probable flow direction (**Figure 8**).*

soft material to protect the equipment and hinder any movement. Despite the increased rectification error, which naturally will affect stereo-matching performance, the rectification error remained below 1 pixel throughout the imaging area, the threshold above which stereo-matching errors become inevitable, since the SDPS stereo matching is performed along lines of 1 pixel width. In the case of significantly impacted camera arrangement, which would have prevented accurate image rectification, it would have been possible to re-calibrate on-site using the

chequerboard (taking approximately 30 minutes), and/or upon return to the laboratory given sufficient camera battery life.

Figure 4A shows the 3D-printed gravel-bed model used for in-situ DEM quality assessment. The chequerboard was used to ensure that the 3D model was placed as horizontal on the ground as possible, facilitating the numerical co-registration of measured and truth data (Bertin et al., 2014). **Figure 4C** shows the DEM of difference (DoD), obtained by differentiating the measured DEM of the 3D-printed model (**Figure 4B**) with the truth DEM, after alignment of the two. Comparison was done on a grid with 0.25 mm spacing; hence at more than 800,000 locations. Visually, large errors (> 10 mm) are rare and are essentially visible at the grains' edges and the troughs of the surface. The measurement of occlusions is a well-known difficulty for both CRDP and TLS (Bertin *et al.*, 2015; Bouratsis *et al.*, 2013; Chandler *et al.*, 2005; Hodge *et al.*, 2009b). Consequently, a general reduction in pore depth and DEM properties such as σ_Z is expected. Quantitatively, most of the measured DEM points (98%) were within ± 3 mm from the truth data, 82% were within ± 1 mm, and 58% were within ± 0.5 mm. σ_Z measured from the DEM was 99.8% of the truth value, showing that surface roughness is reliably measured. From the DoD, a MUE of 0.67 mm between measured and truth values was estimated, with a SDE of 1.16 mm and a maximum unsigned error of 17.1 mm. This is not as good as what can be achieved with CRDP in a laboratory setting (MUE = 0.43 mm, SDE = 0.62 mm and maximum unsigned error of 8.16 mm), with a measuring distance of 640 mm and a 250 mm baseline between the cameras (Bertin et al., 2014). We assume that the deterioration in field DEM quality compared with the laboratory is essentially the result of the increased camera-to-object distance used for image recording, hence degraded horizontal and depth measurement resolutions,

386 and the increased rectification error due to transport. However, this evaluation shows
387 that CRDP can measure exposed fluvial surfaces in the field with sub-millimetre
388 resolution and vertical accuracy (based on MUE), and guarantees reliable grain-
389 scale roughness information from the DEMs. CRDP can even outperform TLS, for

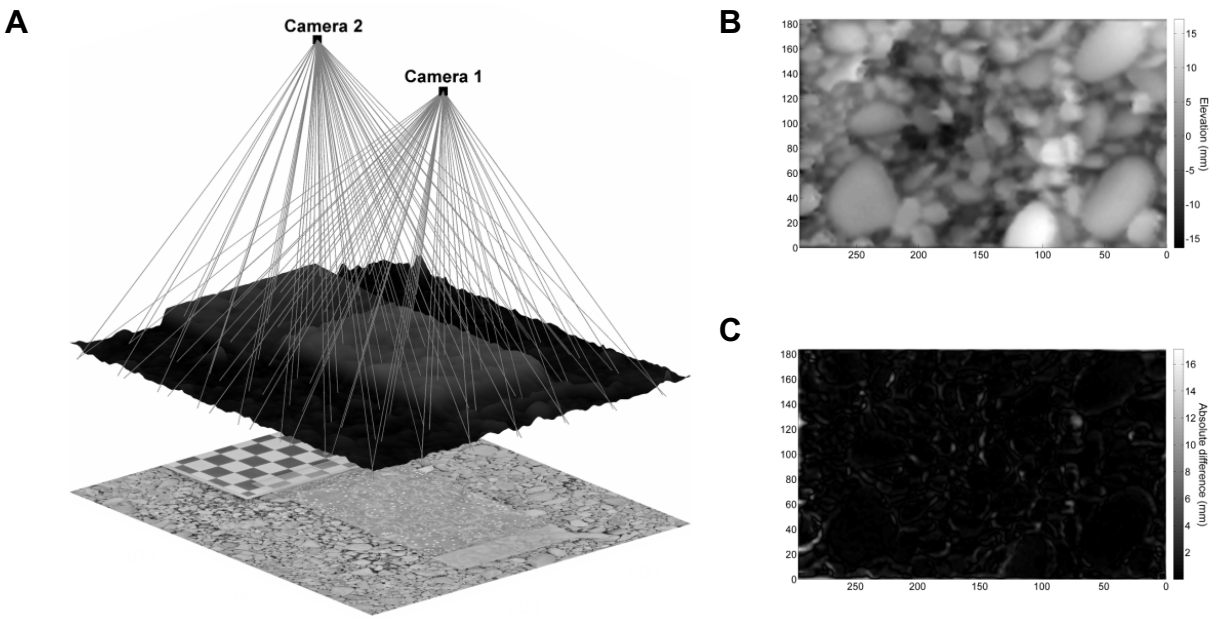

390 ***Figure 4.*** *(A) Close-up presentation of on-site quantitative evaluation of CRDP*
391 *performance using a 3D-printed gravel-bed model; (B) measured DEM of the 3D-*
392 *printed model; and (C) DEM of difference (DoD) between measured and truth data*
393 *(0.25 mm sampling distance).*

394 which a rigorous past application was constrained by the 4 mm laser footprint and
395 resulted in a minimum SDE of ~1.3 mm, after averaging three repeat scans of a
396 plane surface in the laboratory (Hodge et al., 2009b).

397 ### 3.4. DEM analysis

398 **Figure 5A** shows the distribution of (detrended) bed elevations for the three patches.
399 All distributions are positively skewed (S_K = 0.71, 0.53 and 0.52, for bar #1 to #3,
400 respectively), confirming water-worked gravel surfaces (Aberle and Nikora, 2006).

Analysis of the bed-elevation distributions shows that the three patches are different however, and certainly echoes the grain-size differences identified earlier (**Figures 2 and 3)**. Previous studies observed relationships between σ_Z and grain size, generally expressed as D_{50} (Aberle and Nikora, 2006; Hodge et al., 2009a; Smart et al., 2004).

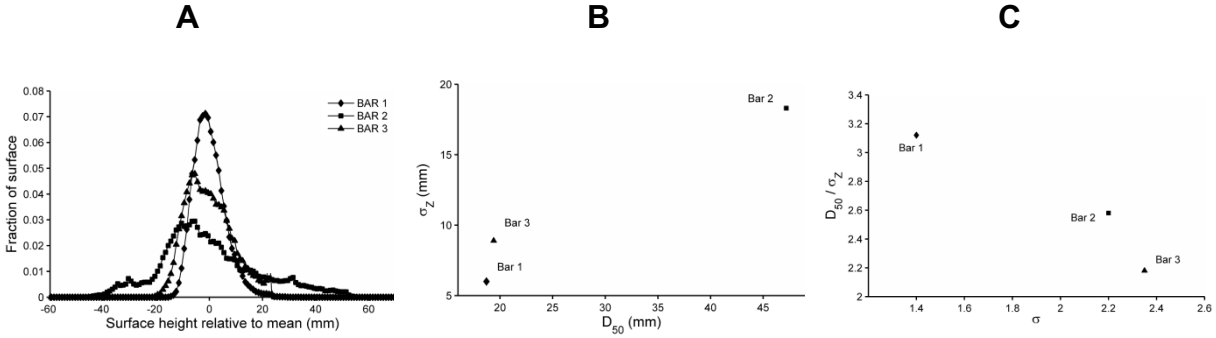

Figure 5. *(A) Distributions of surface elevations for the three patches. Relationships between (B) the standard deviation of bed elevations (σ_Z) and the bed-surface D_{50}; and (C) D_{50}/σ_Z and the sediment geometric sorting (σ).*

Here, bar #1 had the smallest D_{50} and the smallest σ_Z, whilst bar #2 had both the largest D_{50} and σ_Z (**Figure 5B**). However, the ratio of σ_Z to D_{50} (0.32 to 0.46) varied between patches, suggesting that D_{50} is not the only factor determining σ_Z, and other factors such as sediment sorting are also responsible (**Figure 5C**). We found that the ratio D_{50}/σ_Z decreases with the sediment sorting. This suggests that for similar values of D_{50}, poorly-sorted sediments can create more irregular and rougher surfaces, with accentuated grain packing, than well-sorted sediments, which agrees with observations made by Hodge et al. (2009a).

Generalised second-order structure functions of (detrended) bed elevations were calculated for all patches for lags up to ±150 mm (corresponding to 3 to 8 D_{50}, depending on the patch), being always larger than the maximum grain size and enough to reach the saturation region, normalised by the saturation level $2\sigma_Z^2$, and

plotted as 2D isopleth maps (**Figure 6**). Similar to previous work (e.g. Aberle and Nikora (2006)), we found that at small lags (up to 1 D_{50}), the surface structure of the gravel bars is isotropic, as shown by the circular contours in the centre of the isopleth maps. The high correlation between pairs of points at small lags is because

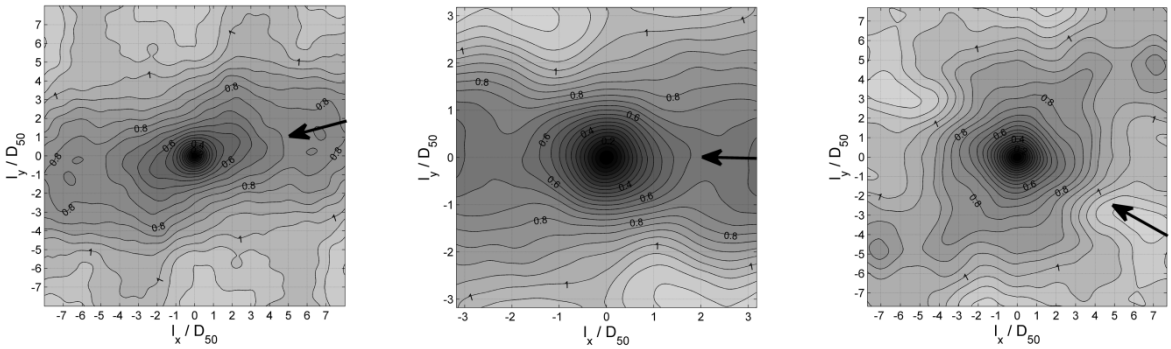

Figure 6. *2D isopleth maps of the generalised second-order structure functions for the three patches (bar #1 to #3 from left to right). The assumed flow direction is along the horizontal axis. Arrows show the most probable flow direction, based on* ***Figure 8****.*

the elevation pairs used to calculate the structure functions belong likely to the same grain, and this suggests that small grains have no prevailing orientation. As the lag increases, the contours generally become elliptical and supposedly reflect the dominant grain orientation, with the long axis of the ellipse representing the *a*-axis alignment (Hodge et al., 2009a; Nikora et al., 1998), until at large lags, equal to 2 to 5 D_{50} depending on the patch, the contours become very irregular. Bar #1 and bar #2 both show a dominant grain orientation with the a-axis parallel to the flow direction. For both patches, the streamwise correlations are stronger than the cross-flow correlations, and remain strong over scales extending over the streamwise size of the plots. This indicates gravelly structures longitudinal to the flow, a common occurrence for water-worked gravel beds in both the laboratory and the field (Aberle

439 and Nikora, 2006; Butler et al., 2001; Cooper and Tait, 2009; Hodge et al., 2009a;
440 Mao et al., 2011). This observation can be attributed to sediment deposition after
441 contact with the upstream front of a stable grain and particle imbrication. Bar #3
442 presents a different shape of structure function for lags up to 2 to 3 D_{50}. This may
443 reflect diamond-shape clusters (Aberle and Nikora, 2006; Mao et al., 2011), whose
444 extensive presence can be noticed on the ortho-image (**Figure 3**), unlike other
445 patches.

446 The combined distributions of DEM cell slope and aspect angles (**Figure 7**) show
447 that all three patches have a dominance of DEM cells with upstream aspects (i.e.
448 aspect angle around 0°). The latter is known to represent particle imbrication (Hodge
449 et al., 2009a), which naturally occurs in a direction parallel to the flow (Laronne and
450 Carson, 1976; Millane et al., 2006). Hence, bar #2 certainly presented the highest
451 rate of surface imbricated grains. From the dominant slope angles in **Figure 7**, the
452 angle of imbrication is estimated at between 25° and 50° for all patches. The three
453 patches however present different grain arrangements at the bed surface. Bar #1 is
454 characterised by DEM cell slopes rarely exceeding 70° and particle imbrication not
455 as pronounced as on bar #2. Bars #2 and #3 have DEM cells with slope angles
456 sometimes reaching 80-90°, indicating more packed particles and rougher surfaces,
457 verifying previously presented observations (**Figure 5)**. Bar #3 shows imbrications
458 over a range of directions, from 0° to 90° with respect to the assumed flow direction.
459 Since imbrication is not centred on zero, which means that surface grains
460 predominantly imbricated in directions different from the flow direction, it might
461 suggest that the flow direction was incorrectly determined in the field. Concurrently,
462 imbricated particles covering a range of directions might say that the flow direction
463 changed over the duration of the last competent event, for example varied with flow

depth, or that different flows (with different directions) imbricated particles in different ways over time, something which was observed in the past (Millane et al., 2006).

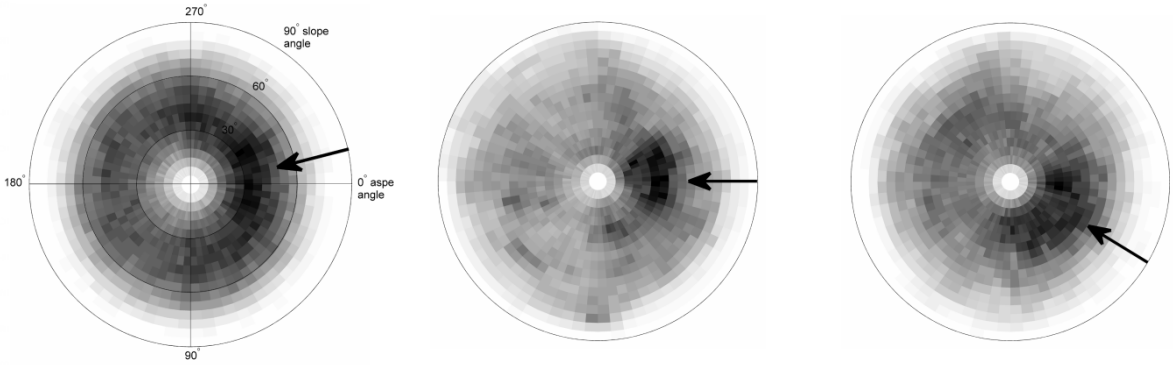

Figure 7. *Polar plots of all 1mm^2 DEM grid cells aspect and slope angles for the three patches (bar #1 to #3 from left to right). Aspect angle is from 0° to 360° and slope angle is from 0° to 90°; plots are shaded by point density (high density in black, zero density in white). The assumed flow direction is from 0° to 180°. Arrows show the most probable flow direction, based on* ***Figure 8****.*

Figure 8 shows the directional inclination indices calculated from the DEMs. Bar #2 shows the largest inclination index; hence, more of the patch area was covered by imbricated particles than on the other patches. This corroborates observations made on the combined distributions of DEM cell slope and aspect angles (**Figure 7**). For bar #2, the inclination index clearly peaks in the direction of the flow, suggesting the flow direction was correctly determined in the field (Millane et al., 2006). Bar #3 has an inclination index that plateaued for angles between approximately 0° and 90°, which again follows observations made previously on **Figure 7**. The maximum inclination index for bar #3 is attained for a DEM direction forming a 30° angle with the flow, suggesting that the assumed flow direction was erroneous by 30° (Millane et al., 2006). If this really is the case, the distribution of DEM cell slope and aspect angles (**Figure 7**) for bar #3, which initially differed from the other two patches,

would have a more natural look and would exhibit a dominance of DEM cells with upstream aspects, hence particle imbrication in the direction of the flow. Likewise, this would affect the measured frequency-distribution of grains' a-axis orientation (**Figure 2B**), which would then peak for angles perpendicular to the flow direction, indicating a dominance of particles reposing across the flow; and the shape of the 2D structure function (**Figure 6**), which would also show a dominant ellipse orientation transverse to the flow direction at medium lags. The latter two observations demonstrate that more particles were aligned transverse to the flow on bar #3 than on the other patches, which can be associated with bedload transport mode by rolling and sliding motion (Laronne and Carson, 1976). Bar #1 shows a smoother distribution of inclination indices, skewed to the left of the plot, which might say that the actual surface-forming flow direction is slightly offset from the assumed flow direction. Whilst this is not as clear as on bar #3, this corroborates observations made on **Figures 6 and 7**.

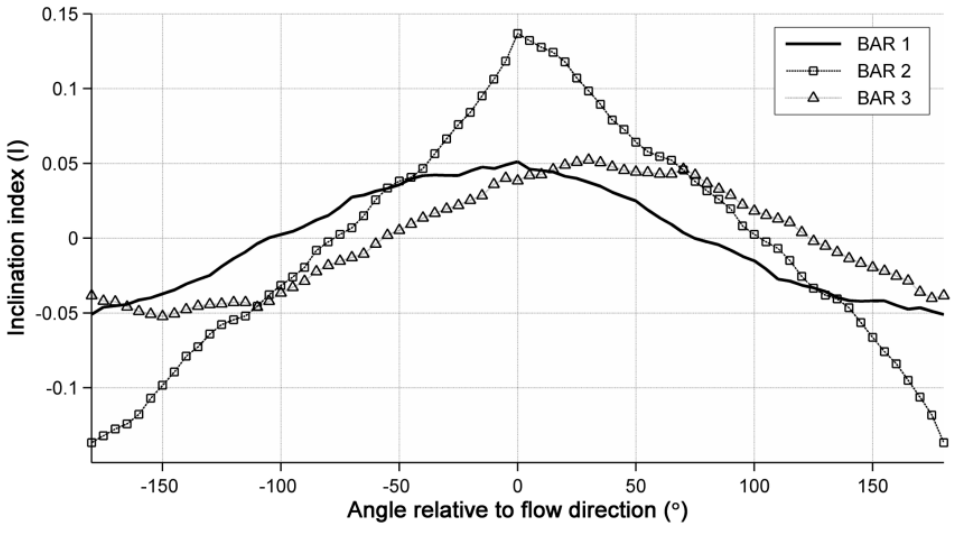

Figure 8. *Directional inclination indices for the three patches. Inclination was calculated for all angles between -180° and 180° at a five-degree interval, using a*

separation distance between pairs of points of 1 mm, which is the DEM sampling distance, the lag for which imbrication was the most perceptible.

4. Discussion

We previously reported on our development of a non-proprietary CRDP technique, making use of consumer-grade digital cameras and off-the-shelf calibration and stereo matching engines, capable of recording gravel beds, water-worked in a laboratory flume, at the grain scale, characterised by sub-millimetre DEM resolution and accuracy (Bertin et al., 2015). We also showed that the same CRDP technique can be used for through-water recording (Bertin et al., 2013). Here, we tested the possibility to deploy the setup and adapt the methodology for measurements in a natural river environment in the field.

4.1. CRDP recommended measurement workflow and field potential

Compared with previous fluvial applications of digital stereo photogrammetry, calibration was performed in one go with a chequerboard, and did not require the placement of fixed control targets on each patch, which in turn would require surveys with a total station (or another independent device) for bundle adjustment. In addition to speeding up data collection and limiting the resources needed on site, calibration with a chequerboard prevents the introduction of additional errors due to the total station, which adversely affects calibration, and hence DEM quality (Carbonneau et al., 2003). It is noted, however, that having fixed control targets of known coordinates (e.g. using a GPS tracker) (i) allows to place measured DEMs within a global coordinate system, (ii) obviates the need to remove trend surfaces (see Section 2.4) and (iii) allows direct surface differencing in sequential surveys, which, however, is deemed unnecessary for small-scale DEMs. For this field work, the application of

524 photogrammetry was rendered even more effective by doing the calibration in “ideal”
525 conditions in the laboratory, providing optimum calibration parameters, prior to
526 moving to the field. There are drawbacks to this method however. The cameras’
527 arrangement on the mounting bar, after calibration, needs to remain as unmodified
528 as possible until the gravel-bed images are collected, to guarantee representative
529 calibration parameters. Using a chequerboard allowed efficient and effective testing
530 of the calibration validity after transport to the field, which was confirmed in this
531 study. Moreover, a laboratory calibration requires pre-supposition of the camera-to-
532 riverbed and baseline distances used in the field, both controlling the measurement
533 performance, and therefore limiting the applicability of the calibrated setup to a range
534 of tasks (microtopographic measurements herewith). With the large body of work on
535 the subject, it is well known that digital cameras are versatile instruments, able to
536 perform 3D measurements over a range of spatial scales, from microtopography to
537 channel shape (Butler et al., 2001; Javernick et al., 2014; Lane, 2000; Lane et al.,
538 2003). The studied scale will depend on the application details. Our CRDP workflow
539 can accommodate various measurement scenarios: (i) several overlapping small-
540 scale DEMs can be merged together, producing a larger DEM that shares the
541 measurement quality of the original DEMs (Bertin et al., accepted for publication); (ii)
542 the CRDP setup can be adjusted and re-calibrated on site to suit larger-scale
543 measurements better (e.g. by increasing the baseline and camera distance); (iii)
544 more than one pre-calibrated setup can be transported to the field, each attributed a
545 specific task; and (iv) a camera can be detached to collect imagery from which
546 larger-scale DEMs are reconstructed using other methods than herewith presented
547 (e.g. SfM, (Javernick et al., 2014)). It is noted that novel SfM/MVS photogrammetric
548 techniques, using a single non-calibrated camera, may provide a viable alternative to

549 classical stereo photogrammetry in measuring gravel patches at fine scales. Some
550 SfM/MVS pipelines are freely available (Stumpf *et al.*, 2015). They are able to
551 generate data at high resolution (James and Robson, 2012) and can begin to tackle
552 the problem of occlusions since imagery is collected from different viewpoints.
553 However, SfM/MVS-generated DEMs may suffer from large non-linear distortions
554 due to inadequate lens distortion calibration (Fonstad *et al.*, 2013; Ouédraogo *et al.*,
555 2014), a drawback that has been resolved in traditional stereo photogrammetry
556 (Bertin *et al.*, 2015; Wackrow and Chandler, 2008). Furthermore, a large number of
557 images (possibly hundreds) are necessary to reach DEM densities comparable to
558 the one required for this study, and will result in much longer processing time (James
559 and Robson, 2012).

560 In conjunction with accurate calibration, scanline-based pixel-to-pixel stereo
561 matching adopted in this study resulted in dense DEMs, with the possibility to have a
562 DEM grid size as small as the pixel size at the riverbed's distance. This fact limited
563 surface smoothing and improved on traditional area-based methods, whereby the
564 smallest DEM grid size is chosen to be five times the pixel size on the surface (Lane
565 et al., 2000). Limited post-processing was applied on the DEMs, which was deemed
566 optional and prevented the introduction of new errors. For TLS applications,
567 measurement resolution can also be a limiting factor for DEM quality. Hodge et al.
568 (2009a; 2009b) reported using a laser-scanning system with a 4 mm footprint in a
569 field study measuring grain-scale fluvial morphology. A rigorous methodology was
570 necessary to maximise point coverage and density and to minimise the effect of the
571 oblique scan angles, by collecting data from two or three scanner positions around
572 each patch, registered together by simultaneously scanning a network of fixed
573 targets, and taking three repeat scans from each scanner position to minimise errors

574 in the data. The reported turn-round time was approximately 25-30 minutes per scan.
575 However, there was still the need of significant post-processing in the form of three
576 filters to obtain accurate metrics (Hodge et al., 2009a; Hodge et al., 2009b; Smith et
577 al., 2012).

578 A potential advantage of TLS over CRDP is its direct “time-of-flight”
579 measurement, compared with measurements relying on image quality and texture
580 (Hodge et al., 2009b). This certainly helped promoting the advent of range (also
581 called time-of-flight) cameras and usage in the Earth Sciences (Mankoff and Russo,
582 2013; Nitsche et al., 2013). However, a number of difficulties, including the need to
583 collect data in low-light conditions, currently limit the applicability of this recent
584 technology in the field and prevent accurate grain-scale data collection. Moreover,
585 surface reflectivity can introduce systematic time-of-flight measurement errors
586 (Hodge et al., 2009b; Nitsche et al., 2013), for which the only remedies are repeat
587 scan processing and filtering. In contrast, digital photogrammetry provides the
588 opportunity to optimise image collection (e.g. by varying the shutter speed), and use
589 image transformation techniques, such as Retinex, to improve stereo matching. This
590 proved to be a source of significant DEM accuracy improvement in the laboratory
591 (Bertin et al., 2015), and we expect this will become even more important in the field,
592 where lighting conditions are variable.

593 During this field work, we also tested the possibility to assess DEM quality
594 without ground check points and a total station. Data quality assessment, an
595 important component to every topographic survey (Lane et al., 2005), was performed
596 using a ground-truth object produced by 3D printing (Bertin et al., 2014). Due to the
597 small size of the 3D-printed model, we believe this assessment suits small-scale
598 DEMs well, but would not be adequate for larger DEMs. In addition to saving time on

599 site, the use of a realistic ground truth provided a precise and reliable quantification
600 of DEM errors. This way, we showed that CRDP is capable of measuring complex
601 surfaces in the field with good vertical accuracy.

602 ### 4.2. Riverbed morphology and between-bar variations

603 A range of methods was used to analyse the gravel-bed DEMs, some of which are
604 by now well-known to the Earth Science community (e.g. probability distribution
605 functions and generalised structure functions), and have been used extensively in
606 studies on the geomorphology of gravel-bed rivers over the past decades (e.g.
607 Robert (1991); Butler et al. (2001); Aberle and Nikora (2006)). Other methods
608 however, such as the combined distribution of DEM cells' slope and aspect angles
609 and the directional inclination index, have only been used in a handful of studies on
610 gravel-bed rivers so far (Hodge et al., 2009a; Millane et al., 2006; Qin et al., 2012).
611 Analysis of surface elevations (**Figure 5**) identified differences between the three
612 patches, and showed that both the median grain size (D_{50}) and sediment sorting (σ)
613 exert control on the surface irregularity and geometric roughness after water-work,
614 with the geometric roughness represented by the standard deviation of bed
615 elevations (σ_Z). The bed-elevation distribution skewness (S_K), positive for all bars,
616 confirmed that the patches comprised water-worked gravels (Aberle and Nikora,
617 2006). Information derived from the 2D structure functions was useful to identify
618 variations on the size, orientation and type of gravel structures found on the gravel
619 bars. Bars #1 and #2 had longitudinal gravel structures, extending over lengths
620 several times the surface D_{50}. Diamond-shaped clusters were observed on bar #3,
621 which was evidenced in the 2D isopleth maps (**Figure 6**). There was a good
622 agreement between the prevailing grain orientation determined using either the
623 structure functions or grain delineation in the photographs (**Figure 2B**). However,

624 this failed at being conclusive on the surface-forming flow direction (Hodge et al.,
625 2009a). The latter is notoriously difficult to determine accurately from visual
626 observations in the field (e.g. Smart *et al*. (2004)). Using DEMs has improved means
627 to determine the antecedent flow direction from measurements of exposed gravel
628 surfaces, especially when relying on surface inclinations (Aberle and Nikora, 2006;
629 Millane *et al.*, 2006; Smart *et al.*, 2004). In this study, analyses of the directional
630 inclination index (**Figure 8**) and the combined distribution of DEM cell slope and
631 aspect angle (**Figure 7**) reached the same conclusion on particle imbrication, hence
632 surface-forming flow direction(s). Bar #2 was the patch with most of its surface
633 covered with imbricated particles (**Figure 8**). The neat imbrication in a single
634 direction confirmed the flow direction determined in the field. Bars #1 and #3
635 presented imbricated particles over a range of directions, suggesting flow direction
636 changed over the last flow event(s) and imbricated particles in different ways.
637 Plotting the directional inclination index has the advantage of clearly showing the
638 angle(s) for which imbrication is the most significant (Millane et al., 2006), hence the
639 surface-forming flow direction(s). Surface slope and aspect is hardly
640 parameterisable, but provides information on the angles with which sediment
641 particles repose at the surface.

642 As Rice and Church (2010) pointed out, focus in past research has been on bed-
643 material grain size variation in gravel-bed rivers at reach and river-length scales, and
644 has sought to explain the principal features, including downstream fining and the
645 gravel-sand transition. Relatively little information is currently available on the
646 variations in surface structure and geometric roughness, despite that we know that
647 these factors influence flow resistance and sediment transport (Church et al., 1998;
648 Komar and Li, 1986; Laronne and Carson, 1976), and may be used to explain the

processes responsible for the formation and evolution of sedimentary units, such as riffles and pools (Hodge et al., 2013). As shown in the presented study, field deployment of remote-sensing techniques, such as CRDP, is becoming easier, and statistical analysis of the DEMs has the potential to provide important information on the variations in surface structure.

5. Conclusion

Collecting information on gravel-bed rivers at the grain scale in both the laboratory and the field, although technically and methodologically challenging, is important for applications such as roughness studies, sediment transport and the interactions between animals and the geomorphology, topics relevant to many river practitioners. Sediment size and 3D arrangement at the riverbed surface are all useful information to collect; these factors control physical processes such as the resistance to the flow, the ability of the flow to entrain sediment and create sediment structures, which in turn can explain the existence of distinct sedimentary units within a river reach, and the large-scale evolution of river basins.

Along with TLS, CRDP is a mature remote-sensing technique, theoretically capable of high-spatial point density and accuracy, necessary for precisely measuring gravel-bed microtopography. Despite extensive applications in the Earth Sciences, both techniques suffer from a tedious measuring workflow when it comes to measure fluvial sediment at the grain scale, which currently hinders the general applicability of these techniques in the field, and in spite of the best of methodological efforts, may not always guarantee reliable findings based on the measured DEMs.

672 This study presented how CRDP can be efficiently deployed in the field to collect
673 high-resolution and high-accuracy DEMs from exposed gravel bars. The only
674 resources needed were two digital cameras mounted on a rigid bar, two tripods and
675 a laptop. Field data collection was greatly simplified by undertaking the necessary
676 calibration in the laboratory, prior to moving to the field. This removed the need to
677 deploy ground-control targets. Dense stereo matching and image optimisation
678 helped the collection of DEMs without being impacted by variable lighting conditions,
679 which challenge applications of TLS and range imaging. A light-weight 3D-printed
680 model, resembling a water-worked gravel bed, was used on site as a ground-truth
681 object to assess the accurate measurement of elevation data. In this work, DEMs
682 were collected at a 1 mm sampling distance, which could go as low as the pixel size
683 at the riverbed's distance (i.e. around 0.25 mm), with a measured accuracy of 0.67
684 mm (based on MUE), which guaranteed reliable grain roughness properties from the
685 DEMs.
686 A variety of statistical methods was applied to the DEMs and identified between-
687 bar sedimentological contrasts. Analysis of the distribution of surface elevations
688 confirmed that the surfaces were water-worked (positive distribution skewness) and
689 allowed ranking the patches by their geometrical roughness (σ_Z). It showed how σ_Z is
690 influenced by both the median grain size (D_{50}) and sediment sorting (σ). Information
691 derived from the 2D structure functions helped identify variations in size, orientation
692 and type of gravel structures found on the gravel bars. Bars #1 and #2 both had
693 longitudinal gravel structures, which contrasted with the diamond-shaped clusters
694 found on bar #3. The prevailing grain orientation determined from automatically
695 delineated grains in the photographs supported observations from the 2D structure
696 functions, but failed at being conclusive on the surface-forming flow direction. For the

latter, analyses of the directional inclination index and the combined distribution of DEM cell slope and aspect angle were the most helpful, showing the direction(s) of particle imbrication, hence the surface-forming flow direction(s).

Continuous progress in topography remote sensing is important to extend our fluvial knowledge, for example by allowing the study of flow-channel processes at different scales, in both space and time. Better characterisation of these processes in situ, with the efficient and effective measurement of submerged surfaces, is a critical task that needs to be tackled in future, ultimately to develop a technique customised for use by fluvial geomorphologists in the field.

References

Aberle, J. and V. Nikora 2006. Statistical properties of armored gravel bed surfaces. *Water Resources Research* 42: W11414.

Aberle, J. and G. M. Smart 2003. The influence of roughness structure on flow resistance on steep slopes. *Journal of Hydraulic Research* 41: 259-269.

Bertin, S. and H. Friedrich Submitted. Stable fluvial armors and surface structure replicability. *Water Resources Research*.

Bertin, S., H. Friedrich and P. Delmas accepted for publication. A merging solution for close-range DEMs to optimise surface coverage and measurement resolution. *Photogrammetric Engineering & Remote Sensing*.

Bertin, S., H. Friedrich, P. Delmas and E. Chan 2013. The use of close-range digital stereo-photogrammetry to measure gravel-bed topography in a laboratory environment, *Proceedings of the 35th IAHR Congress*, Chengdu, China: unpaginated CD-ROM

720 Bertin, S., H. Friedrich, P. Delmas, E. Chan and G. Gimel'farb 2014. DEM quality
721 assessment with a 3D printed gravel bed applied to stereo photogrammetry.
722 *Photogrammetric Record* 29: 241-264.
723 Bertin, S., H. Friedrich, P. Delmas, E. Chan and G. Gimel'farb 2015. Digital stereo
724 photogrammetry for grain-scale monitoring of fluvial surfaces: Error evaluation
725 and workflow optimisation. *ISPRS Journal of Photogrammetry and Remote*
726 *Sensing* 101: 193-208.
727 Bird, S., D. Hogan and J. Schwab 2010. Photogrammetric monitoring of small
728 streams under a riparian forest canopy. *Earth Surface Processes and Landforms*
729 35: 952-970.
730 Bouguet, J.-Y. 2010. http://www.vision.caltech.edu/bouguetj/calib_doc/. (last date
731 accessed: 1st July 2014).
732 Bouratsis, P., P. Diplas, C. L. Dancey and N. Apsilidis 2013. High-resolution 3D
733 monitoring of evolving sediment beds. *Water Resources Research* 49: 977-992.
734 Bradley, D. and W. Heidrich 2010. Binocular camera calibration using rectification
735 error, *Proceedings of the 2010 Canadian Conference on Computer and Robot*
736 *Vision (CRV)*, Ottawa, Ontario, Canada: 183-190
737 Butler, J. B., S. N. Lane and J. H. Chandler 1998. Assessment of DEM quality for
738 characterizing surface roughness using close range digital photogrammetry.
739 *Photogrammetric Record* 16: 271-291.
740 Butler, J. B., S. N. Lane and J. H. Chandler 2001. Characterization of the structure of
741 river-bed gravels using two-dimensional fractal analysis. *Mathematical Geology*
742 33: 301-330.

743 Butler, J. B., S. N. Lane, J. H. Chandler and E. Porfiri 2002. Through-water close
744 range digital photogrammetry in flume and field environments. *Photogrammetric*
745 *Record* 17: 419-439.
746 Carbonneau, P. E., S. N. Lane and N. E. Bergeron 2003. Cost-effective non-metric
747 close-range digital photogrammetry and its application to a study of coarse gravel
748 river beds. *International Journal of Remote Sensing* 24: 2837–2854.
749 Chandler, J., J. Fryer and A. Jack 2005. Metric capabilities of low-cost digital
750 cameras for close range surface measurement. *Photogrammetric Record* 20: 12-
751 26.
752 Church, M., M. A. Hassan and J. F. Wolcott 1998. Stabilizing self-organized
753 structures in gravel-bed stream channels: Field and experimental observations.
754 *Water Resources Research* 34: 3169-3179.
755 Cooper, J. R. and S. J. Tait 2009. Water-worked gravel beds in laboratory flumes - a
756 natural analogue? *Earth Surface Processes and Landforms* 34: 384-397.
757 Detert, M. and V. Weitbrecht 2012. Automatic object detection to analyze the
758 geometry of gravel grains, *Proceedings of the River Flow 2012*, San Jose, Costa
759 Rica (Taylor and Francis Group): 595-600
760 Dowling, T. I., A. Read and J. C. Gallant 2009. Very high resolution DEM acquisition
761 at low cost using a digital camera and free software, *Proceedings of the 18th*
762 *World IMACS Congress and MODSIM09 International Congress on Modelling*
763 *and Simulation* Cairns, Australia: pp. 2479-2485
764 Du Preez, C. and V. Tunnicliffe 2012. A new video survey method of
765 microtopographic laser scanning (MiLS) to measure small-scale seafloor bottom
766 roughness. *Limnology and Oceanography: Methods* 10: 899-909.

767 Entwistle, N. S. and I. C. Fuller 2009. Terrestrial Laser Scanning to Derive Surface
768 Grain Size Facies Character of Gravel Bars. In *Laser Scanning for the*
769 *Environmental Sciences* (eds). Wiley-Blackwell; 102-114
770 Fehr, R. 1987. Geschiebeanalysen in Gebirgsflüssen translated Analysis of
771 Sedimentary Bed Material in Mountain Rivers. Conversion and Comparison of
772 Various Analytical Methods. *Mitteilungen derVersuchsanstalt fürWasserbau,*
773 *Hydrologie und Glaziologie, Eidgenössische Technische Hochschule, Zürich* Nr.
774 92, 1987.
775 Fonstad, M. A., J. T. Dietrich, B. C. Courville, J. L. Jensen and P. E. Carbonneau
776 2013. Topographic structure from motion: a new development in
777 photogrammetric measurement. *Earth Surface Processes and Landforms* 38:
778 421-430.
779 Gimel'farb, G. 2002. Probabilistic regularisation and symmetry in binocular dynamic
780 programming stereo. *Pattern Recognition Letters* 23: 431-442.
781 Graham, D. J., A. J. Rollet, H. Piégay and S. P. Rice 2010. Maximizing the accuracy
782 of image-based surface sediment sampling techniques. *Water Resources*
783 *Research* 46: W02508.
784 Hannam, M. and M. L. Moskal 2015. Terrestrial Laser Scanning Reveals Seagrass
785 Microhabitat Structure on a Tideflat. *Remote Sensing* 7: 3037-3055.
786 Hauer, C., G. Unfer, P. Holzapfel, M. Haimann and H. Habersack 2014. Impact of
787 channel bar form and grain size variability on estimated stranding risk of juvenile
788 brown trout during hydropeaking. *Earth Surface Processes and Landforms* 39:
789 1622-1641.
790 Heritage, G. L. and D. J. Milan 2009. Terrestrial Laser Scanning of grain roughness
791 in a gravel-bed river. *Geomorphology* 113: 4-11.

792 Hodge, R., J. Brasington and K. Richards 2009a. Analysing laser scanned digital
793 terrain models of gravel bed surfaces: linking morphology to sediment transport
794 processes and hydraulics. *Sedimentology* 56: 2024-2043.
795 Hodge, R., J. Brasington and K. Richards 2009b. In situ characterization of grain-
796 scale fluvial morphology using Terrestrial Laser Scanning. *Earth Surface*
797 *Processes and Landforms* 34: 954-968.
798 Hodge, R. A., D. A. Sear and J. Leyland 2013. Spatial variations in surface sediment
799 structure in riffle–pool sequences: a preliminary test of the Differential Sediment
800 Entrainment Hypothesis (DSEH). *Earth Surface Processes and Landforms* 38:
801 449-465.
802 James, M. R. and S. Robson 2012. Straightforward reconstruction of 3D surfaces
803 and topography with a camera: Accuracy and geoscience application. *Journal of*
804 *Geophysical Research: Earth Surface* 117: n/a-n/a.
805 James, T. D., P. E. Carbonneau and S. N. Lane 2007. Investigating the effects of
806 DEM error in scaling analysis. *Photogrammetric Engineering & Remote Sensing*
807 73: 67-78.
808 Javernick, L., J. Brasington and B. Caruso 2014. Modeling the topography of shallow
809 braided rivers using Structure-from-Motion photogrammetry. *Geomorphology*
810 213: 166-182.
811 Komar, P. D. and Z. Li 1986. Pivoting analyses of the selective entrainment of
812 sediments by shape and size with application to gravel threshold. *Sedimentology*
813 33: 425-436.
814 Lane, S. N. 2000. The measurement of river channel morphology using digital
815 photogrammetry. *Photogrammetric Record* 16: 937-961.

816 Lane, S. N., T. D. James and M. D. Crowell 2000. Application of digital
817 photogrammetry to complex topography for geomorphological research.
818 *Photogrammetric Record* 16: 793-821.
819 Lane, S. N., S. C. Reid, R. M. Westaway and D. M. Hicks 2005. Remotely sensed
820 topographic data for river channel research: the identification, explanation and
821 management of error. In *Spatial Modelling of the Terrestrial Environment* (eds).
822 John Wiley & Sons, Ltd; 113-136
823 Lane, S. N., R. M. Westaway and D. Murray Hicks 2003. Estimation of erosion and
824 deposition volumes in a large, gravel-bed, braided river using synoptic remote
825 sensing. *Earth Surface Processes and Landforms* 28: 249-271.
826 Laronne, J. B. and M. A. Carson 1976. Interrelationships between bed morphology
827 and bed-material transport for a small, gravel-bed channel. *Sedimentology* 23:
828 67-85.
829 Mankoff, K. D. and T. A. Russo 2013. The Kinect: a low-cost, high-resolution, short-
830 range 3D camera. *Earth Surface Processes and Landforms* 38: 926-936.
831 Mao, L., J. R. Cooper and L. E. Frostick 2011. Grain size and topographical
832 differences between static and mobile armour layers. *Earth Surface Processes*
833 *and Landforms* 36: 1321-1334.
834 Millane, R. P., M. I. Weir and G. M. Smart 2006. Automated Analysis of Imbrication
835 and Flow Direction in Alluvial Sediments Using Laser-Scan Data. *Journal of*
836 *Sedimentary Research* 76: 1049-1055.
837 Nelson, P. A., W. E. Dietrich and J. G. Venditti 2010. Bed topography and the
838 development of forced bed surface patches. *Journal of Geophysical Research:*
839 *Earth Surface* 115: n/a-n/a.

840 Nikora, V. I., D. G. Goring and B. J. F. Biggs 1998. On gravel-bed roughness
841 characterization. *Water Resources Research* 34: 517-527.
842 Nitsche, M., J. M. Turowski, A. Badoux, D. Rickenmann, T. K. Kohoutek, M. Pauli
843 and J. W. Kirchner 2013. Range imaging: a new method for high-resolution
844 topographic measurements in small- and medium-scale field sites. *Earth Surface*
845 *Processes and Landforms* 38: 810-825.
846 Ouédraogo, M. M., A. Degré, C. Debouche and J. Lisein 2014. The evaluation of
847 unmanned aerial system-based photogrammetry and terrestrial laser scanning to
848 generate DEMs of agricultural watersheds. *Geomorphology* 214: 339-355.
849 Qin, J., D. Zhong, G. Wang and S. L. Ng 2012. On characterization of the imbrication
850 of armored gravel surfaces. *Geomorphology* 159–160: 116-124.
851 Rice, S. P. and M. Church 2010. Grain-size sorting within river bars in relation to
852 downstream fining along a wandering channel. *Sedimentology* 57: 232-251.
853 Rice, S. P., M. F. Johnson and I. Reid 2012. Animals and the Geomorphology of
854 Gravel-Bed Rivers. In *Gravel-Bed Rivers* (eds). John Wiley & Sons, Ltd; 225-241
855 Rieke-Zapp, D. H., R. Rosenbauer and F. Schlunegger 2009. A photogrammetric
856 surveying method for field applications. *Photogrammetric Record* 24: 5-22.
857 Robert, A. 1991. Fractal properties of simulated bed profiles in coarse-grained
858 channels. *Mathematical Geology* 23: 367-382.
859 Rüther, N., S. Huber, S. Spiller and J. Aberle 2013. Verifying a photogrammetric
860 method to quantify grain size distribution of developed armor layers, *Proceedings*
861 *of the 35th IAHR Congress*, Chengdu, China: 7
862 Smart, G., J. Aberle, M. Duncan and J. Walsh 2004. Measurement and analysis of
863 alluvial bed roughness. *Journal of Hydraulic Research* 42: 227-237.

Smith, M., D. Vericat and C. Gibbins 2012. Through-water terrestrial laser scanning of gravel beds at the patch scale. *Earth Surface Processes and Landforms* 37: 411-421.

Smith, M. W. and D. Vericat 2013. Evaluating shallow-water bathymetry from through-water terrestrial laser scanning under a range of hydraulic and physical water quality conditions. *River Research and Applications*.

Stumpf, A., J. P. Malet, P. Allemand, M. Pierrot-Deseilligny and G. Skupinski 2015. Ground-based multi-view photogrammetry for the monitoring of landslide deformation and erosion. *Geomorphology* 231: 130-145.

Verdú, J. M., R. J. Batalla and J. A. Martínez-Casasnovas 2005. High-resolution grain-size characterisation of gravel bars using imagery analysis and geo-statistics. *Geomorphology* 72: 73-93.

Wackrow, R. and J. H. Chandler 2008. A convergent image configuration for DEM extraction that minimises the systematic effects caused by an inaccurate lens model. *Photogrammetric Record* 23: 6-18.

Wackrow, R., J. H. Chandler and P. Bryan 2007. Geometric consistency and stability of consumer-grade digital cameras for accurate spatial measurement. *Photogrammetric Record* 22: 121-134.